

Research Article

Envelope-Based Variable-Gain Control Strategy for Vibration Suppression of Solar Array Using Reaction Wheel Actuator

Song Wu,^{1,2} Guoan Tang,¹ and Bifa Chen³ 

¹Department of Aeronautics and Astronautics, Fudan University, Shanghai 200433, China

²Shanghai Key Laboratory of Spacecraft Mechanism/Shanghai Institute of Aerospace System Engineering, Shanghai 201109, China

³School of Aerospace Engineering, Xiamen University, Xiamen, Fujian 361102, China

Correspondence should be addressed to Bifa Chen; bfchen@xmu.edu.cn

Received 10 January 2022; Revised 12 April 2022; Accepted 15 April 2022; Published 20 May 2022

Academic Editor: Jiafu Liu

Copyright © 2022 Song Wu et al. This is an open access article distributed under the Creative Commons Attribution License, which permits unrestricted use, distribution, and reproduction in any medium, provided the original work is properly cited.

The orbital operation of spacecraft can excite the long-drawn and low-frequency vibration of the solar array, which is prone to affecting the task execution of the system. To address this issue, an envelope-based variable-gain control strategy is proposed to suppress vibration of the solar array using the reaction wheel (RW) actuator. The RW actuator is individually mounted on the solar array to provide reaction torque through the speed change of its rotor. The governing equation of motion of the solar array actuated by a RW actuator is deduced with the state space representation. The control relation between the measured bending moment and the rotational speed of the RW actuator with the constant-gain coefficient is firstly developed and demonstrated in numerical simulation. Changing the gain coefficient to be inversely proportional to the envelope function of vibration, a variable-gain control strategy is proposed to improve the damping effect of the RW actuator. Simulation results show that the vibration suppression performance of the RW actuator is improved compared to the constant-gain control. As the actual on-orbit natural frequency of the solar array is not always exactly known, the robustness of the control system is analyzed for the deviation between the estimated and the actual natural frequency values. The proposed variable-gain control is also experimentally verified using a simplified elastic plate model. Experimental results indicate that the vibration attenuation time is decreased to 29.1% and 50.22% compared to the uncontrolled and the constant-gain controlled states, respectively.

1. Introduction

With the trend of larger expansion in dimensions, the deployable appendages of the spacecraft, such as the solar array, the antenna, and the manipulator, possess remarkable flexibility in a fully deployed state [1, 2]. The ultralow natural frequency of the large-scale flexible appendage f_n is the main reason for slow vibration attenuation. The vibration can result from various on-orbit excitations, e.g., the spacecraft's attitude adjusting, the payload pointing, and the spacecraft docking [3–5]. Besides, due to the absence of air resistance and weak friction between mechanisms under low gravity, the inherent modal damping ratio ζ_n of the appendage is quite small. According to the exponential law of vibration attenuation, for vibration amplitude decaying by ζ times, the required time is estimated by $-\ln \zeta / (2\pi f_n \zeta_n)$. If the empirical values of f_n and ζ_n are taken as 0.05 Hz

and 0.005, respectively, and the required $\zeta = 5\%$, then the required time is 1907.1 s. In such cases, it takes a long time to sufficiently attenuate the excited vibration, which is unfavorable for the spacecraft attitude control and payload accurate pointing. In addition, the longtime vibration may accumulate mechanical damage to the flexible appendages.

Various methods have been developed to suppress the vibration of the spacecraft's flexible appendages in the last decades. These methods can mainly be divided into the feed-forward control such as the input shaping technique, the passive vibration control (PVC), and the active vibration control (AVC). The input shaping technique was applied to reduce the vibration of the appendages during spacecraft orbital maneuvering, solar array sun pointing, or manipulator transporting [6, 7]. For example, Na et al. [4] used the built-in actuator at the array base to control the vibration of a solar array. However, the input shaping technique does

not work when the structural vibration direction is different from the actuating direction of the built-in actuator. Moreover, it is not suitable for accelerating the residual vibration attenuation of the structure.

Adopting the passive or active control method satisfied the needs of accelerating vibration attenuation [8–11]. By applying damping materials or passive dampers to the structures, the passive control methods were implemented and demonstrated to be highly stable and efficient [12–14]. However, for the large-scale flexible appendages, the partially covered damping materials or passive dampers are not able to efficiently improve the low-order modal damping of the whole system. The active control methods perform well by combining a network of sensor-controller-actuator and provide a significant vibration suppression effect [15–17]. The actuator selection for different application situations is one of the issues in AVC. Piezoelectric material is a type of widely used actuator [18–20]. It is also employed as the sensor in active control [21–24]. However, the suppression effect is not obvious when the piezoelectric actuator is applied to large-scale flexible space structures. To solve this issue, Casella et al. [25] combined both the piezoelectric material and the on-off air jet thrusters as the actuators, but the compensation of the air jet working medium of the thrusters is an obstacle in space application. Sun et al. [26] proposed a novel vibration suppression scheme for solar arrays by using the cable-driven parallel robot actuators, which achieved a remarkable vibration suppression effect. Whereas for the deployable space structures, the involved cables cause issues in deploying process design. Meanwhile, its robustness is also an issue in practical application. Hu et al. [27] used a stiffness-variable joint mechanism for two hinged flexible plates. Both simulation and experimental results demonstrated the significant damping effect induced by the innovative joint mechanism. However, the actuator is only suitable for the sort of flexible structures embedded with joint mechanisms.

The reaction wheel (RW) is usually implemented in spacecraft attitude control, which has the benefits of light weight and high efficiency with consumption of renewable electricity [28–32]. An active control method to suppress the vibration of the solar array through the RW actuator was studied in [33]. Numerical simulations of a solar array showed that, by using a RW actuator with approximately 2% of the structural mass, the vibration attenuation time was reduced to one-third of that from the uncontrolled state. However, for aerospace applications, the requirements of the RW actuator, such as the volume and weight, are very strict. Therefore, it is desirable to maximize the actuator's vibration suppression capability. The sliding mode control [34, 35], the fuzzy logic [36], and the artificial algorithm [37] were investigated and integrated into the vibration control strategy design for the space flexible appendages. Bonding the piezoelectric actuator to the flexible panel, Liu et al. [38] developed a hybrid control scheme for the attitude stabilization and vibration suppression of the flexible spacecraft by considering model parameter uncertainty, measurement error, actuator faults, and other factors. It is worth pointing out that finding the optimal gains for the controller is very

crucial and challenging for achieving the best performance of vibration suppression in the control system, which is still an open research problem. The variable gain control methods have been developed by other researchers in various engineering applications previously [39–43]. Combining the variable gain control into the design of a vibration suppression strategy has the potential in improving the damping performance of the actuators. Due to the fact that the gain adjustment rules require complex procedures and the calculations of the relevant parameters usually depend on experience [44–46], it is challenging to construct a feasible variable-gain control strategy for AVC in actual implementation.

In this paper, we focus on developing a variable gain control strategy for the RW actuator to maximize its capability in suppressing vibration of the solar array. The main contribution of this paper is the variable-gain control strategy through the envelope function of vibration to improve the damping performance of the RW actuator for vibration suppression of the solar array. The numerical models of a full-scale solar array with variable-gain control and constant-gain control are developed to evaluate and validate the proposed algorithm. An elastic plate model is used in the laboratory for feasibility investigation. The design, implementation, and verification of the proposed strategy are presented to highlight the significant vibration suppression performance of the RW actuator. The control relation between the measured bending moment and the rotational speed of the RW actuator with the constant gain is firstly applied to the solar array. It is figured out from the simulation results that a larger amplitude of the rotational speed of the RW actuator implies a larger output reaction torque in the control, which leads to a better damping effect. In our work, adjusting the control gain to be linear to the inverse of the vibration envelope is the strategy to increase the output reaction torque of the RW actuator. The proposed variable-gain control strategy is proved to be able to improve the damping performance of the RW actuator compared to the constant-gain control.

The rest of the paper is organized as follows. In Section 2, dynamic modelling for vibration suppression of the solar array by utilizing the RW actuator is deduced, and the damping effect of the RW actuator is demonstrated through a full-scale flexible solar array with numerical simulation. The design, numerical verification, and robustness analysis of the envelope-based variable-gain control strategy are discussed in Section 3. Experimental results are presented in Section 4 to illustrate the effectiveness and feasibility of the presented method. Conclusions are drawn in Section 5.

2. Dynamic Modelling and Effect of Vibration Suppression for Solar Array

2.1. Vibration Suppression for Solar Array Utilizing RW Actuator. For vibrating structures dominated by the first-order mode, the physical quantities describing the structural motion state can be approximately expressed by the modal coordinate ξ_1 and its corresponding modal shape function φ , in which ξ_1 is a temporal function and φ is a spatial function. For example, as shown in Figure 1, the solar array has

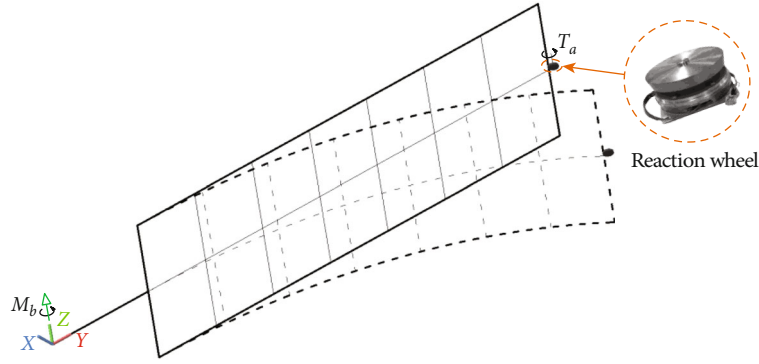


FIGURE 1: Structural diagram of the solar array with a RW actuator.

the geometric characteristic of a large length-to-width ratio. The root of the solar array connecting to the spacecraft body is fixed based on the assumption that the mass and moment of inertia of the spacecraft body are much larger than that of the solar array [47]. For the sake of illustration, a Cartesian coordinate system is established on the solar array. The X -axis is parallel to the normal direction of the panel surface. The Y -axis is parallel to the extension direction. The Z -axis follows the right-hand rule. In this paper, the first-order out-of-plane bending mode of the solar array along the X -axis is assumed to be dominant.

To suppress the first-order out-of-plane bending vibration, a RW actuator is mounted at the midspan of the free side of the solar array, as shown in Figure 1. The reaction torque induced by the speed change of the RW actuator is applied as the active force. The angular displacement around the Z -axis at the RW mounted position is designated as θ . The root bending moment M_b is defined as the moment around the Z -axis at the connected position between the root of the flexible solar array and the spacecraft body. Both M_b and θ can be expressed as linear functions of the modal coordinate ξ_1 .

Denoting the linear proportionality coefficients as φ_M and φ_θ , M_b and θ can be written as

$$\begin{aligned} M_b &= \varphi_M \xi_1, \\ \theta &= \varphi_\theta \xi_1, \end{aligned} \quad (1)$$

respectively. Such that

$$M_b = \frac{\varphi_M}{\varphi_\theta} \theta. \quad (2)$$

The control law for the rotational speed of RW Ω is designed to be proportional to the root bending moment M_b :

$$\Omega = \eta M_b = \eta \varphi_M \xi_1. \quad (3)$$

The rotating axis of Ω is parallel to the Z -axis. The control gain η can be given by

$$\eta = \frac{\Omega_{\max}}{M_{b,\max}} = \frac{\Omega_{\max}}{\theta_{\max}} \frac{\varphi_\theta}{\varphi_M}. \quad (4)$$

Here, Ω_{\max} denotes the permitted maximum rotational speed of the RW actuator; the peak values of θ , M_b during vibration are θ_{\max} , $M_{b,\max}$, respectively. Specifying η by Equation (4) results that the RW actuator rotates at Ω_{\max} when the structural vibration reaches the peak with no overload.

Denoting the rotational acceleration of the RW as $\dot{\Omega}$, according to the moment of momentum theorem, the induced reaction torque applied to the solar array is $T_a = -I\dot{\Omega}$. Considering Equation (3), the reaction torque T_a can be written as

$$T_a = -I\eta\dot{M}_b, \quad (5)$$

in which I is the rotating moment of inertia of the RW about its rotational axis. Controlling the rotational speed Ω by the designed algorithm, the induced torque T_a can be used to suppress the vibration of the solar array.

Performing a first-order time derivative on both sides of Equation (2) and substituting the result into Equation (5) by considering Equation (4) gives

$$T_a = -I \frac{\Omega_{\max}}{\theta_{\max}} \dot{\theta}. \quad (6)$$

The minus sign “-” guarantees the direction of the reaction torque T_a always opposite to the direction of the angular velocity $\dot{\theta}$. As a result, the RW actuator can always do negative work to the solar array. That is, T_a plays a role of consuming the vibration mechanical energy of the solar array, so it can be regarded as artificial damping.

The motion equation of the flexible solar array with a RW actuator can be expressed in the first-order modal coordinate as

$$\ddot{\xi}_1 + 2\omega_1\zeta_1\dot{\xi}_1 + \omega_1^2\xi_1 = \varphi_\theta T_a. \quad (7)$$

Here, ω_1 and ζ_1 are the first-order natural frequency (rad/s) and modal damping ratio, respectively. The detailed

derivation of Equation (7) can be consulted from [33]. Rewriting Equation (7) in a state-space representation:

$$\dot{\mathbf{x}} = \mathbf{A}\mathbf{x} + \mathbf{B}\mathbf{u}, \quad (8)$$

where

$$\begin{aligned} \mathbf{x} &= \begin{bmatrix} \dot{\xi}_1 & \xi_1 \end{bmatrix}^T, \\ \mathbf{u} &= [T_a], \\ \mathbf{A} &= - \begin{bmatrix} 2\omega_1\zeta_1 & \omega_1^2 \\ -1 & 0 \end{bmatrix}, \\ \mathbf{B} &= [\varphi_\theta \quad 0]^T. \end{aligned} \quad (9)$$

They can be referred to as the state vector (\mathbf{x}), the input vector (\mathbf{u}), the state matrix (\mathbf{A}), and the input matrix (\mathbf{B}), respectively.

On the other hand, Equation (1) can be equivalently written as

$$\mathbf{y} = \mathbf{C}\mathbf{x}, \quad (10)$$

where

$$\begin{aligned} \mathbf{y} &= [M_b], \\ \mathbf{C} &= [0 \quad \varphi_M]. \end{aligned} \quad (11)$$

Here, \mathbf{y} and \mathbf{C} are the output vector and the output matrix, respectively.

Equation groups (8) and (10) are the typical state-space form of a dynamic system [48]. The abovementioned modal parameters can be obtained by numerical approach, e.g., finite element method.

2.2. Numerical Simulations and Analysis. The solar array with a deployed area of 6.2 m × 25 m utilized in the Tianhe core module of the Chinese Space Station is adopted to validate the effectiveness of the vibration control method. The corresponding finite element model with a full scale is constructed using MSC/PATRAN, and it is shown in Figure 2.

The flexible panels are meshed by shell elements. The driving mechanisms, the deployable structures, and the storing tubes and boxes are modelled using beam elements with measured physical parameters. Interested readers can consult Reference [49] for more detailed information. A torsional spring element with a modulus of 10⁶ N · m/rad is employed to connect the root of the solar array and the spacecraft body. The end of the spring element with connection to the spacecraft body is fixed. The finite element mesh (blue grid) and its first-order out-of-plane bending vibration mode are shown in Figure 2. The modal analysis is performed with MSC/NASTRAN. The total mass of the solar array model is 594.2 kg. The RW actuator selected in the simulation weighed 1 kg, which accounted for about 0.17% of the model in this study case. The moment of inertia of

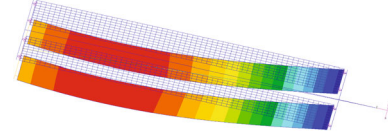


FIGURE 2: The finite element mesh of the flexible solar array and its first-order bending mode.

the current RW is 0.005 kg · m². The maximum rotational speed is 6000 RPM, i.e., $\Omega_{\max} = 628.3$ rad/s.

The modal parameters of the full-size flexible solar array model utilized in the numerical simulation are listed as follows. The first-order natural frequency of the model is $\omega_1 = 0.2746$ rad/s. The modal parameters mentioned in Equation (1) are $\varphi_M = 29.15$ N · m and $\varphi_\theta = 0.003$ rad, respectively. Considering the testing experiences for similar structures, the modal damping ratio of the model is taken as $\zeta_1 = 0.005$ (very small as suggested by the aerospace agency).

To make the simulation more realistic, a band-pass filter is adopted for the sensor signal to eliminate the DC (direct current) drift and high-frequency noise. The band-pass filter is a 2nd-order Butterworth filter with a high cut-off frequency of 0.06118 Hz and a low cut-off frequency of 0.02622 Hz. Namely, the band width of the filter is determined through taking the first-order bending natural frequency of the solar array as the central frequency and floating up and down by 40%. The constant-gain control law expressed in Equation (3) is firstly employed to verify the vibration suppression effect. The simulation process is executed with a fixed-step size of 0.01 s. The peak value of the root bending moment is approximately 150 N · m once disturbed. Thus, the initial conditions of the model are given by

$$\xi_1(0) = 0, \dot{\xi}_1(0) = 1.5 \text{ s}^{-1}. \quad (12)$$

As shown in Figure 3, the controller realized by Equation (3) is involved to obtain the speed signal for the RW actuator. The control gain is 3.76 N · m · s/rad given by Equation (4). If the gain coefficient is 0, the reaction torque T_a equals to 0 during the whole simulation process, which can be regarded as the state without control.

The simulation results of the bending moment M_b with and without control are plotted as the solid and the dashed lines in Figure 4, respectively. Compared to the dashed line (without control), the attenuation of the solid line (with control) is accelerated. The comparison demonstrates that the reaction torque T_a can be used to suppress the vibration of the solar array through designing the rotational speed Ω according to the control law given by Equation (3).

The rotational speed Ω is shown in Figure 5. It is much larger and close to its permitted maximum value Ω_{\max} in the early stage. However, according to Equations (3) and (5), the peak values of Ω and the reaction torque T_a decrease with the attenuation of vibration. For example, the rotational speed of the RW decays to 267.4 rad/s at 384.3 s, which is

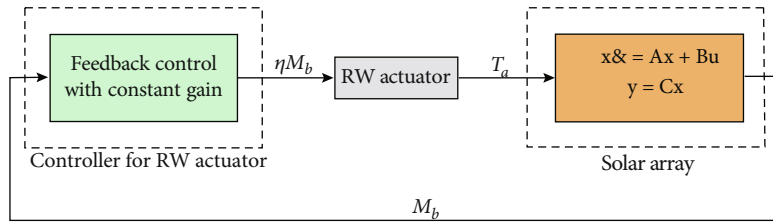


FIGURE 3: Diagram of the feedback control with constant gain.

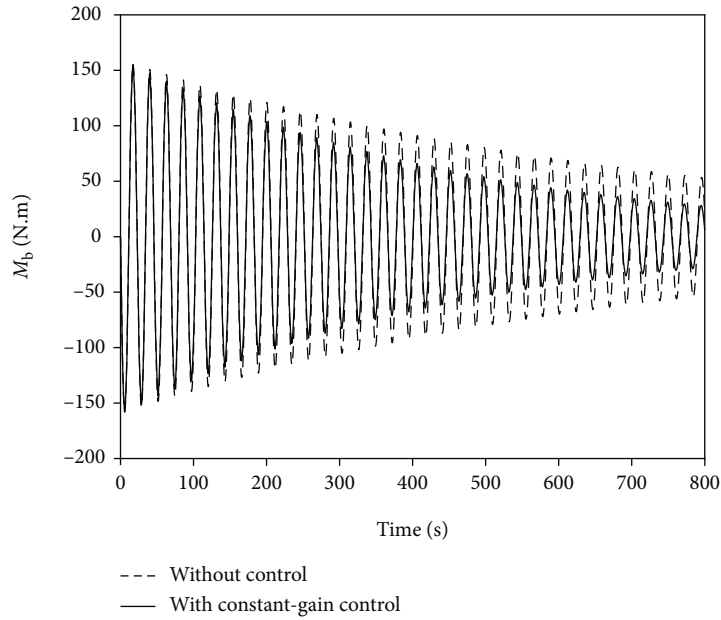


FIGURE 4: Response curve of the root bending moment with constant-gain control.

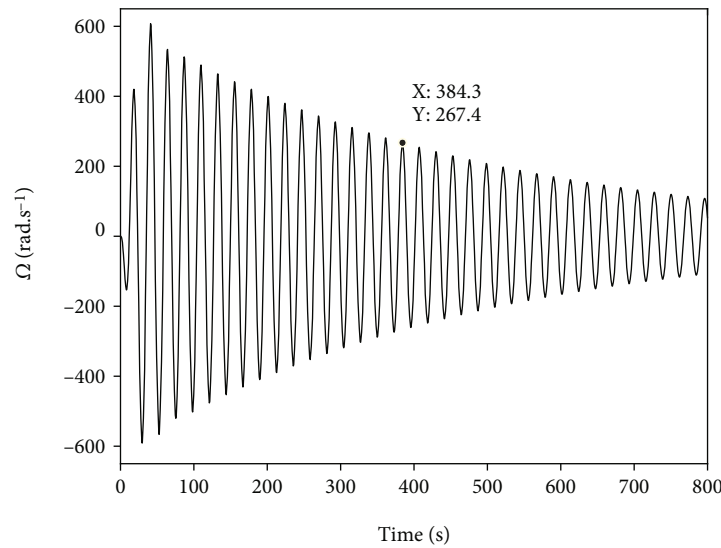


FIGURE 5: Rotational speed of the RW actuator with constant-gain control.

less than half of Ω_{\max} . In this paper, the amplitude of the rotational speed is defined as a measure of the capability of the RW actuator utilized for vibration suppression. A larger

amplitude of the rotational speed, which is closer to Ω_{\max} , is preferred, for which the capability of the RW actuator is more sufficiently utilized to provide a better control effect.

Hence, it indicates that the capability of the RW actuator has the potential to be improved for providing a better control effect.

3. Design, Simulation, and Analysis of Envelope-Based Variable-Gain Control

To overcome the issue that the amplitude of the rotational speed decreases with the attenuation of vibration, it is proposed to involve a variable-gain control algorithm based on the envelope function of vibration in the feedback control law. The controller design, as well as the numerical verification and the robustness analysis of the control system, is going to be discussed in this section.

3.1. Controller Design. With the action of the damping force (i.e., the inherent structural damping and the reaction torque), vibration amplitude of the solar array decreases over time with a given initial condition. The envelope of the root bending moment M_b gradually converges to 0 from $M_{b,\max}$. Hence, determining the gain coefficient η according to Equation (4) guarantees Ω not exceed its permitted limit in the beginning of the control. Whereas the structure vibration amplitude decreases, amplifying the gain coefficient also makes the RW operate in the permitted operating range. For example, the relationship of M_b and Ω can be redesigned as

$$\Omega = \gamma \eta M_b. \quad (13)$$

Here, γ is the design factor to amplify the gain coefficient appropriately.

The control effect of the RW decreases with the vibration attenuation by adopting the constant-gain control. Inspired by that, the gain amplifying coefficient γ can be designed to be linear to the inverse of the envelope function of vibration. The response of the bending moment $M_b(t)$ in the time domain presents the characteristics of periodic vibration and relatively slow attenuation. The slow attenuation part is the so-called envelope function in mathematics, and it can be denoted as $\mathcal{E}[M_b(t)]$. During the free vibration attenuation, the ideal envelope function of the root bending moment $\mathcal{E}[M_b(t)]$ is a monotonically decreasing function with a maximum value $M_{b,\max}$. The reciprocal of $\mathcal{E}[M_b(t)]$ is a monotonically increasing function. Therefore, the amplifying coefficient γ is accordingly designed as

$$\gamma = \frac{M_{b,\max}}{\mathcal{E}[M_b(t)]}. \quad (14)$$

Considering Equation (4), Equation (14) can be described as

$$\gamma = \frac{\Omega_{\max}}{\eta \mathcal{E}[M_b(t)]} = \frac{\Omega_{\max}}{\mathcal{E}[\eta M_b(t)]}. \quad (15)$$

To avoid the exception that the denominator (i.e., $\mathcal{E}[M_b(t)]$) is zero in the numerical calculations, the maximum value of γ should be limited. A simple way is to apply a hard-

bound γ_{\max} to the computation of γ . Substituting Equation (15) into Equation (13), M_b and Ω are linked via

$$\Omega = \min \left(\frac{\Omega_{\max}}{\mathcal{E}[\eta M_b(t)]}, \gamma_{\max} \right) \times \eta M_b(t). \quad (16)$$

In the digital signal process, the envelope function can be computed by various methods, such as Hilbert transform [50, 51] or squaring and low-pass filtering [52, 53]. In this research, the envelope of the measured response signal is solved by using the squaring and low-pass filtering method. Designate the envelope function $\mathcal{E}[M_b(t)] = \bar{M}$. If the low-pass filter is taken as a 2nd-order Butterworth low-pass filter with a cutoff frequency Ω_p (rad/s), the squaring of \bar{M} in the Laplace domain satisfies [54]

$$\mathcal{L}[N] = G(s)\mathcal{L}[2M_b^2] = \frac{2\Omega_p^2}{s^2 + \sqrt{2}\Omega_p s + \Omega_p^2} \mathcal{L}[M_b^2], \quad (17)$$

in which $\mathcal{L}[\cdot]$ denotes the Laplace transformation, $G(s)$ is the transfer function of the filter, and s is the Laplace variable,

$$N = \bar{M}^2. \quad (18)$$

Rewriting Equation (17) in the time domain:

$$\ddot{N} + \sqrt{2}\Omega_p \dot{N} + \Omega_p^2 N = 2\Omega_p^2 M_b^2. \quad (19)$$

Performing the first- and second-order time derivatives on both sides of Equation (18), respectively, we have

$$\dot{N} = 2\bar{M}\dot{\bar{M}}, \quad \ddot{N} = 2\bar{M}\ddot{\bar{M}} + 2\dot{\bar{M}}^2. \quad (20)$$

Substituting Equations (18) and (20) into Equation (19), the relation of \bar{M} and M_b can be constructed:

$$2\bar{M}\ddot{\bar{M}} + 2\dot{\bar{M}}^2 + \sqrt{2}\Omega_p 2\bar{M}\dot{\bar{M}} + \Omega_p^2 \bar{M}^2 = 2\Omega_p^2 M_b^2. \quad (21)$$

Unit Equations (13) and (14) to eliminate γ :

$$M_b = \frac{\Omega \bar{M}}{\eta \Omega_{\max}}. \quad (22)$$

Substituting Equation (22) into Equation (21) and moving the item on the right-hand side of the equation to the left-hand side lead to

$$\ddot{\bar{M}} + \frac{1}{\bar{M}} \dot{\bar{M}}^2 + \sqrt{2}\Omega_p \dot{\bar{M}} + \frac{\Omega_p^2}{2} \bar{M} - \frac{\Omega_p^2 \Omega^2 \bar{M}}{\eta^2 \Omega_{\max}^2} = 0. \quad (23)$$

Then, substituting the first equation of Equation (1) into Equation (22),

$$\frac{\Omega \bar{M}}{\eta \Omega_{\max}} = \varphi_M \xi_1. \quad (24)$$

Recalling Equation (24), one can get

$$\Omega = \eta \Omega_{\max} \varphi_M \frac{\xi_1}{\bar{M}}, \dot{\Omega} = \eta \Omega_{\max} \varphi_M \left(\frac{\dot{\xi}_1}{\bar{M}} - \frac{\xi_1 \dot{\bar{M}}}{\bar{M}^2} \right). \quad (25)$$

Simultaneous formulas (5), (7), (23), and (25), the equation group of the closed-loop system is constituted by ξ_1 and \bar{M} :

$$\begin{cases} \ddot{\xi}_1 + 2\omega_1 \zeta_1 \dot{\xi}_1 + \omega_1^2 \xi_1 = a \left(\frac{\dot{\xi}_1 \dot{\bar{M}}}{\bar{M}^2} - \frac{\dot{\xi}_1}{\bar{M}} \right), \\ \ddot{\bar{M}} + \sqrt{2} \Omega_p \dot{\bar{M}} + \frac{\Omega_p^2}{2} \bar{M} = \frac{b}{\bar{M}} \xi_1^2 - \frac{1}{\bar{M}} \dot{\bar{M}}^2, \end{cases} \quad (26)$$

where $a = I \Omega_{\max}^2 \varphi_{\theta}^2 / \theta_{\max}$, $b = \Omega_p^2 \varphi_M^2$, and $a, b > 0$.

Designating $\{y_1 \ y_2 \ y_3 \ y_4\}^T = \{\dot{\xi}_1 \ \xi_1 \ \dot{\bar{M}} \ \bar{M}\}^T$, the equation group (26) can be written equivalently as follows:

$$\begin{cases} \dot{y}_1 = -2\omega_1 \zeta_1 y_1 - \omega_1^2 y_2 + a \frac{y_2 y_3}{y_4^2} - a \frac{y_1}{y_4}, \\ \dot{y}_3 = -\sqrt{2} \Omega_p y_3 - \frac{\Omega_p^2}{2} y_4 + \frac{b}{y_4} y_2^2 - \frac{1}{y_4} y_3^2. \end{cases} \quad (27)$$

Perform a Taylor expansion of function y_4 at time t_0 , and denote $y_4 = y_{40} + \Delta y_4$ ($y_{40} > 0$), where Δy_4 is the corresponding small increment. Then,

$$\begin{aligned} \dot{y}_4 &= \Delta \dot{y}_4, \\ \frac{1}{y_4} &= \frac{1}{y_{40} + \Delta y_4} = \frac{1}{y_{40}} \frac{1}{1 + \Delta y_4 / y_{40}} \approx \frac{1}{y_{40}} \left(1 - \frac{\Delta y_4}{y_{40}} \right), \\ \frac{1}{y_4^2} &= \frac{1}{y_{40}^2} \left(1 - \frac{\Delta y_4}{y_{40}} \right)^2 \approx \frac{1}{y_{40}^2} \left(1 - 2 \frac{\Delta y_4}{y_{40}} \right). \end{aligned} \quad (28)$$

Substituting Equation (28) into Equation (27), and adding two identical equations $\dot{y}_2 = y_1$ and $\Delta \dot{y}_4 = y_3$, one can obtain

$$\begin{cases} \dot{y}_1 = -2\omega_1 \zeta_1 y_1 - \omega_1^2 y_2 + \frac{a}{y_{40}^2} y_2 y_3 - \frac{a}{y_{40}} y_1 - \frac{2a}{y_{40}^3} y_2 y_3 \Delta y_4 - \frac{a}{y_{40}^2} y_1 \Delta y_4, \\ \dot{y}_2 = y_1, \\ \dot{y}_3 = -\sqrt{2} \Omega_p y_3 - \frac{\Omega_p^2}{2} y_{40} + \frac{b}{y_{40}} y_2^2 - \frac{1}{y_{40}} y_3^2 + \frac{1}{y_{40}^2} y_3^2 \Delta y_4 - \frac{\Omega_p^2}{2} \Delta y_4 - \frac{b}{y_{40}^2} y_2^2 \Delta y_4, \\ \Delta \dot{y}_4 = y_3. \end{cases} \quad (29)$$

Considering the assumption of small perturbation and weak damping, y_1, y_2, y_3 , and Δy_4 are small quantities. Thus, neglecting the higher-order terms, the corresponding state-space representation of Equation (29) can be built up:

$$\dot{y}_s = \mathbf{A}_s y_s + \mathbf{B}_s u_s. \quad (30)$$

Here,

$$\mathbf{A}_s = \begin{bmatrix} -\left(2\omega_1 \zeta_1 + \frac{a}{y_{40}}\right) & -\omega_1^2 & \mathbf{0} & \\ 1 & 0 & & \\ & & \mathbf{0} & -\sqrt{2} \Omega_p & -\frac{\Omega_p^2}{2} \\ & & & 1 & 0 \end{bmatrix},$$

$$y_s = \begin{bmatrix} y_1 \\ y_2 \\ y_3 \\ \Delta y_4 \end{bmatrix}, \quad (31)$$

$$\mathbf{B}_s = \begin{bmatrix} 0 \\ 0 \\ 1 \\ 0 \end{bmatrix},$$

$$u_s = -\frac{\Omega_p^2}{2} y_{40} = \text{constant},$$

in which $\mathbf{0}$ is a 2×2 zero matrix.

The characteristic equation of the closed-loop system (30) is

$$\left[\lambda^2 + \left(2\omega_1 \zeta_1 + \frac{a}{y_{40}} \right) \lambda + \omega_1^2 \right] \left[\lambda^2 + \sqrt{2} \Omega_p \lambda + \frac{\Omega_p^2}{2} \right] = 0. \quad (32)$$

The solutions of Equation (32) are

$$\begin{aligned} \lambda_{1,2} &= \frac{-(2\omega_1 \zeta_1 + a/y_{40}) \pm \sqrt{(2\omega_1 \zeta_1 + a/y_{40})^2 - 4\omega_1^2}}{2}, \\ \lambda_{3,4} &= -\frac{\sqrt{2}}{2} \Omega_p. \end{aligned} \quad (33)$$

It can be seen from Equation (33) that the real parts of λ_i ($i = 1, 2, 3, 4$) are negative, and it is independent of y_{40} . Or, namely, the system is stable with a local Taylor expansion of y_4 at any time such that the stability in the whole process can be guaranteed. Thus, the closed-loop system is stable in small perturbation.

3.2. Numerical Verification. In this section, to make the different control strategies comparable, the numerical model of the flexible solar array, as shown in Figure 2, is used to examine the effect of the proposed variable-gain control strategy.

The feedback control diagram with envelope-based variable-gain control is updated based on Figure 3, and it is shown in Figure 6. The gain amplifying coefficient γ , which is constructed according to Equation (15), is involved in the controller to improve the reaction torque provided by

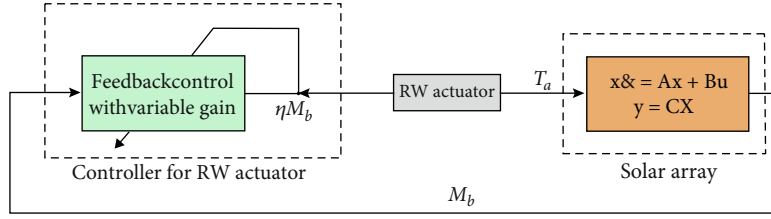


FIGURE 6: Diagram of the feedback control with variable gain.

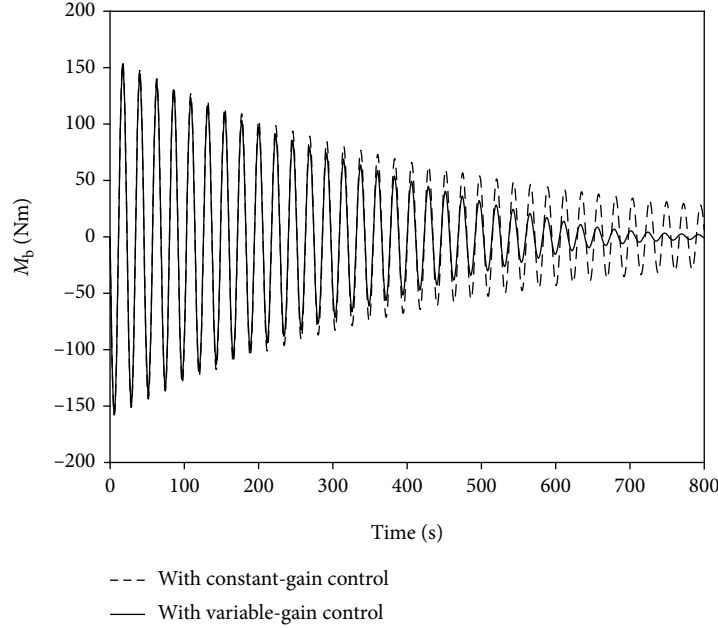


FIGURE 7: Response curve of the root bending moment with variable-gain control.

the RW actuator. The bound γ_{\max} is taken as 10 in this study. There is a delay in calculating the envelope function of the response signal by using the squaring and low-pass filtering method. The correct envelope value of the signal is output at about the second natural period of vibration after the simulation starts. Therefore, the rotational speed Ω should be limited in case exceeding its permitted operating range. To this end, a saturation module is utilized to limit the absolute value of its output within Ω_{\max} , which is also applied to the negative values of Ω .

The transient responses are revisited with the same initial condition, as shown in Equation (12). Figure 7 reveals two response curves of M_b , in which the black bold line and the black dashed line are the responses with envelope-based variable-gain and constant-gain control, respectively. Compared to the response with constant-gain control, the vibration attenuation speed with envelope-based variable-gain control is increased, which verifies the effectiveness of the proposed approach. Taking the threshold as 5% of $M_{b,\max}$, the time required for vibration amplitude damping to the threshold is called vibration attenuation time. The vibration attenuation times in different cases are listed in

TABLE 1: The vibration attenuation times of the simulation model.

	Without control	Constant-gain control	Variable-gain control
Vibration attenuation time (s)	2181.7	1367.6	657.5

Table 1. As shown, the result with constant-gain control is 1367.6s, which is reduced to 657.5s when adopting envelope-based variable-gain control. That is, the vibration attenuation time with variable-gain control is decreased to 48.1% from the state with constant-gain control and to 30.1% from the state without control.

The rotational speed Ω with envelope-based variable-gain control is shown in Figure 8. As seen, in the first 600 s, the RW actuator rotates at a peak value near Ω_{\max} , which implies the output reaction torque is improved. Therefore, involving the variable-gain control algorithm enables us to maximize the capability of the RW actuator and improve its damping effect.

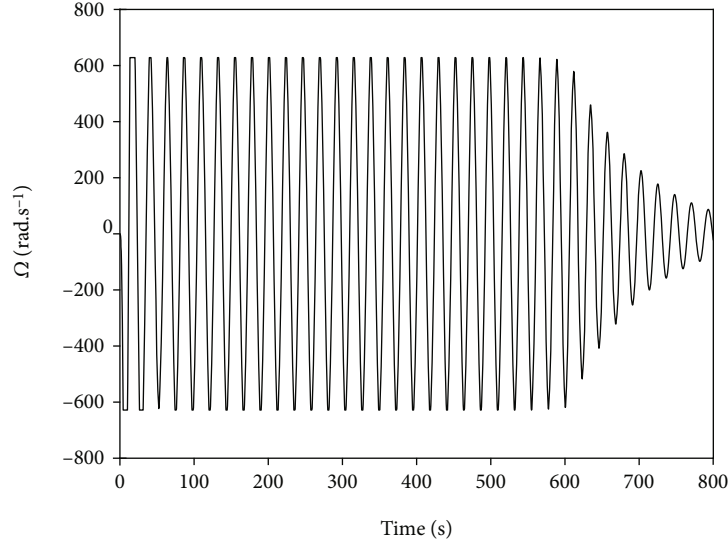


FIGURE 8: Rotational speed of the RW with variable-gain control.

3.3. Robustness Analysis. The envelope-based variable-gain control strategy is designed and verified for the configuration of the solar array characterized by nominal parameters. However, once the spacecraft is orbiting, some of its structural characteristics can result different from the ones measured during ground tests or derived from a numerical model. Among all the possible uncertainties, the ones that have a major impact on the performance of the vibration suppression of the solar array are associated with the natural frequency. In the following, these uncertainties reflect on the estimated errors of the first-order bending natural frequency, which result in the effect of the capability of the proposed control strategy to reduce the vibrations. Taking $\omega_1 = 0.2746$ rad/s as the benchmark, it is assumed that the predetermined frequency for the control system design exists relative errors of $\pm 5\%$, $\pm 10\%$, $\pm 15\%$, and $\pm 20\%$, respectively. Adopting the method mentioned above, the high cut-off and the low cut-off frequencies of the band-pass filter are redesigned under different frequency error settings. The corresponding transient responses of the solar array are revisited with the same model and initial conditions.

Compared to the vibration attenuation time $t_0 = 2181.7$ s without control, the vibration attenuation times with control and their relative ratios to t_0 (i.e., relative attenuation time) under different estimated error settings are listed in Table 2. From Table 2, the vibration suppression still works effectively when the predetermined frequency deviates to a certain extent from the exact frequency (0.2746 rad/s). It reveals that the control system is robust when there are errors in the predetermined frequency. Unfortunately, if the error is too large, for example, an error of -20% , the relative attenuation time is only decreased to 52.16%. Therefore, in order to achieve a better vibration suppression effect, it is advisable to provide the natural frequency of the solar array as accurately as possible.

TABLE 2: Vibration suppression effect under different relative error conditions.

	Relative error	Vibration attenuation time (s)	Relative attenuation time (%)
1	0	657.5	30.14
2	5%	670.3	30.72
3	-5%	713.4	32.70
4	10%	671.1	30.76
5	-10%	779.4	35.72
6	15%	672.7	30.84
7	-15%	901.8	41.34
8	20%	696.0	31.90
9	-20%	1137.9	52.16

4. Experimental Verification

4.1. Experimental Setup for Vibration Suppression. In this section, a real example is used for feasibility investigation. The test article is an elastic plate with two additional weights. Figure 9 details the experimental setup. The anti-shock sponges with a thickness of 0.5 mm are pasted on both surfaces of the plate. The two additional weights and anti-shock sponges are utilized to adjust the natural frequency and damping of the model, respectively. To reduce the influence of gravity, the plate is laterally placed to ensure that the bending vibration is perpendicular to the gravity direction. One side of the elastic plate is fixed on a sliding table to simulate the disturbance from the spacecraft body. The other side is equipped with a brushed-DC motor (BDCM), which serves as a RW actuator to provide reaction torque.

In this case, the total mass of the DC motor is 5.8 g. Parameters of the experimental apparatus are listed in Table 3. By experimental test and analysis, the natural

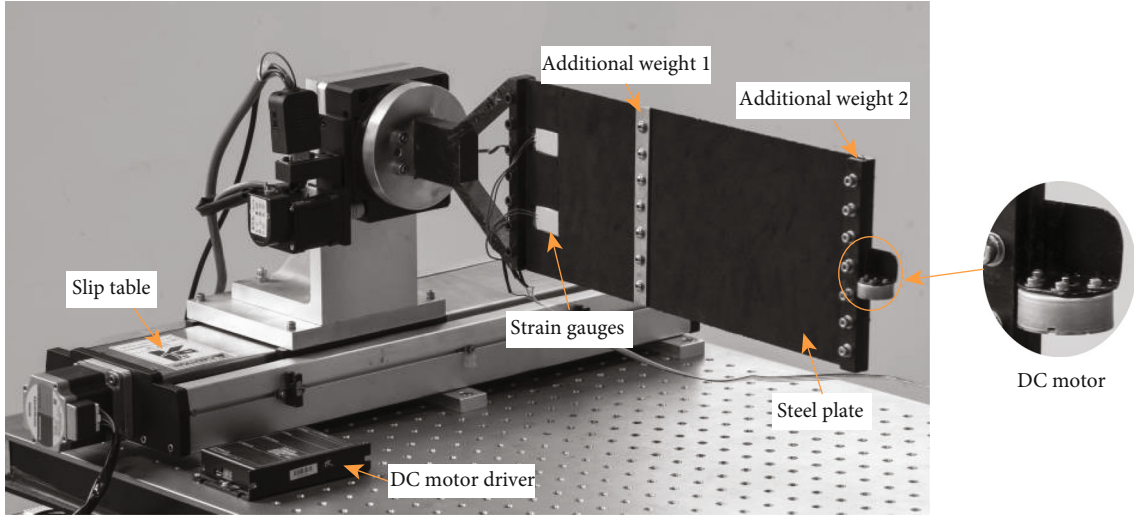


FIGURE 9: Photograph of the experimental setup for vibration suppression.

TABLE 3: Parameters of the experimental apparatus.

Length, height, and thickness of elastic plate	370 mm × 150 mm × 0.3 mm
Mass of elastic plate	126 g
Mass of additional weight 1	67 g
Mass of additional weight 2	115 g
Distance from fixed side to additional weight 1	217.5 mm
Distance from fixed side to additional weight 2	362.5 mm
Mass of DC motor	5.8 g

frequency corresponding to the first-order out-of-plane bending mode of the model is 0.805 Hz.

Instead of measuring the bending moment as done in the numerical simulation, in the experiment, the strain signal of the vibrating structure is measured to acquire the input of the control system. To acquire the signal with a larger SNR (signal-to-noise ratio), the measuring point is arranged at a location with higher stresses. Denote the longitudinal strain of the measured position as ε_l , then the modal coordinate can be solved by

$$\xi_1(t) = \frac{\varepsilon_l}{\varphi_\varepsilon}, \quad (34)$$

where φ_ε is the first-order modal coefficient corresponding to ε_l . Meanwhile, Equation (34) indicates that the measured strain signal is proportional to ξ_1 . Therefore, according to Equations (3) and (34), the rotational speed and the measured strain signal can be linked via

$$\Omega = \frac{\eta\varphi_M}{\varphi_\varepsilon} \varepsilon_l. \quad (35)$$

Equation (35) states that similar to measuring the root bending moment M_b , the measured strain signal is linear to the speed signal of the RW actuator in the experiment. However, it should be noted that Equation (35) holds, if and only if the linear relationships exist between the modal coordinate and M_b, ε_l , as stated in Equations (1) and (34).

The strain gauges, with a resistance of 350 Ω , are bonded on the elastic plate near the fixed side to acquire the local strain signal ε_l . The input voltage of the full-bridge strain circuit is 1.5 V. The output voltage of the strain bridge circuit is amplified 3000 times linearly by a strain amplifier and sampled by an analog-to-digital (A/D) module. Let V_ε be the strain amplifier's output voltage, which is also called strain voltage. Through the A/D module, the corresponding digital value of V_ε is acquired and regarded as the input of the control system.

When the elastic plate is disturbed, V_ε changes with the vibration of the elastic plate. According to the pre-designed algorithm, the driving signal voltage V_d commanding the speed of the DC motor is solved and output to the motor driver through a D/A (digital-to-analog) module. In this paper, the motor driver is ESCON-50/5 produced by MAXON Corporation. The speed signal voltage range is 0 ~ 2.4 V, corresponding to the rotational speed 0~14800 RPM linearly. The direction of the rotational speed is commanded by a logic high or low signal.

The slip table administrated by a stepper motor is adopted to excite the vibration of the elastic plate model. The excitation is performed as follows. The slip table undergoes two periods of sinusoidal motion at 0.8 Hz along the normal direction of the plate surface. The speed function v_e of the excitation table is given in mm/s by

$$v_e = \begin{cases} 15 \sin(1.6\pi t), & 0 \leq t \leq 2.5 \text{ s}, \\ 0, & t > 2.5 \text{ s}. \end{cases} \quad (36)$$

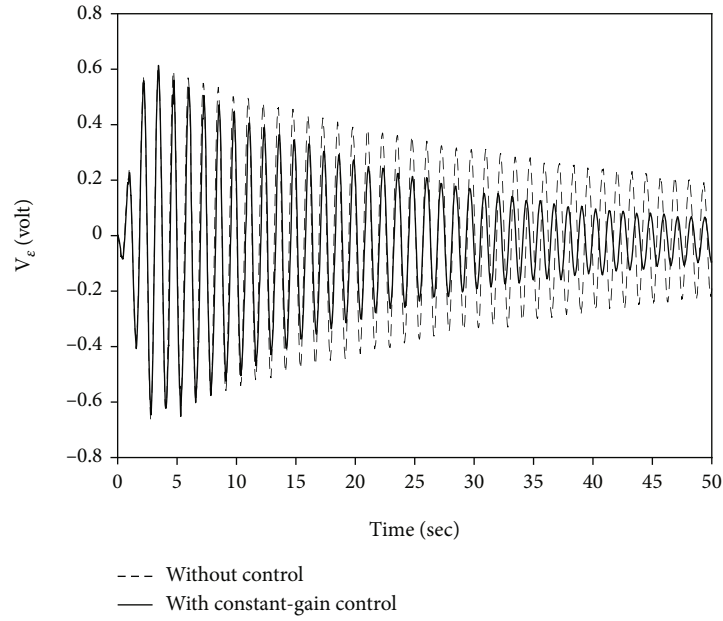


FIGURE 10: Measured response curve of the strain voltage with constant-gain control.

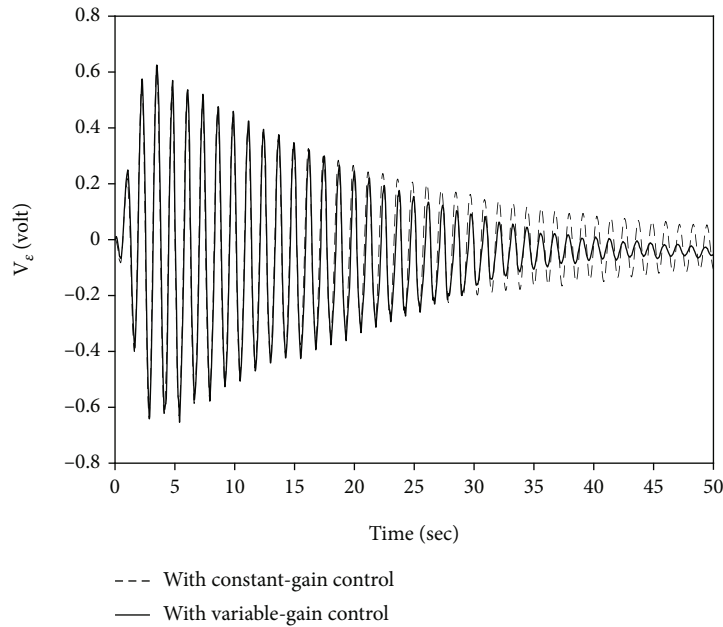


FIGURE 11: Measured response curve of the strain voltage with variable-gain control.

The vibration response is measured by strain gauges during the entire time period (from the beginning of the excitation to the end of the experiment). In order to verify the suppression effectiveness, the vibration attenuation with and without control is measured.

4.2. *Experimental Performance of Vibration Suppression Subjected to Different Control Strategies.* As aforementioned, the rotational speed Ω and the strain ϵ , are linear to the electric voltage V_d and V_ϵ , respectively. Recalling Equation (35),

the driving signal voltage V_d is proportional to the strain voltage V_ϵ :

$$V_d = \kappa V_\epsilon, \tag{37}$$

where κ is the proportional gain coefficient in the experiment. It is required that the motor rotates within the maximum ratings and near the maximum speed when V_ϵ reaches its peak value. Therefore, the coefficient κ is estimated by $V_d^{\max}/V_\epsilon^{\max}$, and it is taken as -3.5 in this case, in

TABLE 4: The vibration attenuation time of the experiment model.

	Without control	Constant-gain control	Variable-gain control
Vibration attenuation time (s)	153.4	89	44.7

which V_d^{\max} is the permitted maximum value of the driving voltage, which equals to 2.4 V in this case.

The response curve of the strain voltage V_ε with constant-gain control is shown as the solid line in Figure 10. Compared to the response without control (the dashed line), the vibration attenuation process is accelerated. The results verify that the vibration attenuation of the elastic plate can be accelerated by applying the reaction torque based on the control relation (37).

The envelope-based variable-gain control strategy is also validated based on the elastic plate model. Recalling Equations (15) and (16), the gain amplifying coefficient γ in the experiment is accordingly designed to be

$$\gamma = \min \left(\frac{V_d^{\max}}{\mathcal{E}[\kappa V_\varepsilon(t)]}, \gamma_{\max} \right). \quad (38)$$

The calculation module for γ is added to the control program according to Equation (38). The envelope-based variable-gain control strategy is employed for vibration suppression of the plate model with the same experimental settings. The response curve of the strain voltage V_ε is plotted as the solid line in Figure 11. Compared to the measured result with constant-gain control (the dashed line), the attenuation speed with the proposed variable-gain control is increased.

The vibration attenuation time is used as a metric to demonstrate the vibration suppression efficiency. The vibration amplitude threshold $V_\varepsilon^* = 0.05 \mathcal{E}^{\max}[V_\varepsilon(t)]$. Based on the measured responses, the vibration attenuation times without control, with constant-gain control, and with envelope-based variable-gain control are listed in Table 4, respectively. Compared to 153.4 s and 89 s, the vibration attenuation time with envelope-based variable-gain control is reduced to 29.1% of that from the uncontrolled state and to 50.22% of that from the constant-gain controlled state.

5. Conclusion

In this paper, an envelope-based variable-gain control strategy for the reaction wheel (RW) actuator is proposed to suppress the bending vibration of the solar array. Both numerical simulations and experimental studies are provided to demonstrate the rationality and validity of the proposed variable-gain control in improving the vibration suppression performance of the RW actuator compared to the constant-gain control. Taking the finite element model of a full-scale solar array as the object, the damping effects of the RW actuator subjected to different control strategies are compared by using the vibration attenuation time as a metric. The vibration attenuation time without control and

with constant-gain control are 2181.7 s and 1367.6 s, respectively, and it is reduced to 657.5 s when the envelope-based variable-gain control is adopted. The numerical simulations considering deviations between the estimated and the exact natural frequency values are performed to analyze the robustness of the control system. It is concluded that the proposed technique is robust within a deviation range of $\pm 20\%$. To obtain a better control effect, a more accurate estimation value of the natural frequency is required. Experiments on an elastic plate model further prove that the proposed variable-gain control method is a valid and feasible technology. Compared to 153.4 s and 89 s, the vibration attenuation time with envelope-based variable-gain control is reduced to 29.1% of that from the uncontrolled state and to 50.22% of that from the constant-gain controlled state.

Data Availability

The data used to support the findings of this study are available from the corresponding author upon request.

Conflicts of Interest

The authors declared no potential conflicts of interest with respect to the research, authorship, and/or publication of this article.

Acknowledgments

This research is supported by the Open Project of Shanghai Key Laboratory of Spacecraft Mechanism (Grant No. 18DZ2272200).

References

- [1] J. Santiago-Prowald and H. Baier, "Advances in deployable structures and surfaces for large apertures in space," *CEAS Space Journal*, vol. 5, no. 3-4, pp. 89-115, 2013.
- [2] E. Wang, S. Wu, G. Xun, Y. Liu, and Z. Wu, "Active vibration suppression for large space structure assembly: a distributed adaptive model predictive control approach," *Journal of Vibration and Control*, vol. 27, pp. 365-377, 2020.
- [3] B. A. Albassam, "Fast attitude maneuver of a flexible spacecraft with passive vibration control using shunted piezoelectric transducers," *International Journal of Aerospace Engineering*, vol. 2019, 2019.
- [4] S. Na, G.-A. Tang, and L.-F. Chen, "Vibration reduction of flexible solar array during orbital maneuver, aircraft engineering and aerospace technology: an," *International Journal*, vol. 86, pp. 155-164, 2014.
- [5] K. Shi, C. Liu, Z. Sun, and X. Yue, "Coupled orbit-attitude dynamics and trajectory tracking control for spacecraft electromagnetic docking," *Applied Mathematical Modelling*, vol. 101, pp. 553-572, 2022.
- [6] H. Yavuz, S. Mistikoğlu, and S. Kapucu, "Hybrid input shaping to suppress residual vibration of flexible systems," *Journal of Vibration and Control*, vol. 18, no. 1, pp. 132-140, 2012.
- [7] H. Ghorbani, K. Alipour, B. Tarvirdizadeh, and A. Hadi, "Comparison of various input shaping methods in rest-to-rest motion of the end-effector of a rigid-flexible robotic

- system with large deformations capability,” *Mechanical Systems and Signal Processing*, vol. 118, pp. 584–602, 2019.
- [8] Q. Hu and G. Ma, “Spacecraft vibration suppression using variable structure output feedback control and smart materials,” *Journal of Vibration and Acoustics*, vol. 128, pp. 221–230, 2005.
- [9] X.-Y. Mao, H. Ding, and L.-Q. Chen, “Passive isolation by nonlinear boundaries for flexible structures,” *Journal of Vibration and Acoustics*, vol. 141, no. 5, 2019.
- [10] L. Zhang, S. Xu, Z. Zhang, and N. Cui, “Active vibration suppression for flexible satellites using a novel component synthesis method,” *Advances in Space Research*, vol. 67, pp. 1968–1980, 2020.
- [11] P. Tarazaga, D. Inman, and W. Wilkie, “Control of a space rigidizable-inflatable boom using embedded piezoelectric composite actuators,” in *47th AIAA/ASME/ASCE/AHS/ASC Structures, Structural Dynamics, and Materials Conference*, p. 1976, Newport, RI, USA, 2006.
- [12] T. P. Sales, D. A. Rade, and L. C. G. de Souza, “Passive vibration control of flexible spacecraft using shunted piezoelectric transducers,” *Aerospace Science and Technology*, vol. 29, no. 1, pp. 403–412, 2013.
- [13] M. Bodaghi, M. Shakeri, and M. Aghdam, “Passive vibration control of plate structures using shape memory alloy ribbons,” *Journal of Vibration and Control*, vol. 23, no. 1, pp. 69–88, 2017.
- [14] S. Bhattarai, H. Kim, and H.-U. Oh, “CubeSat’s deployable solar panel with viscoelastic multilayered stiffener for launch vibration attenuation,” *International Journal of Aerospace Engineering*, vol. 2020, Article ID 8820619, 10 pages, 2020.
- [15] Y. Xie, H. Shi, F. Bi, and J. Shi, “A MIMO data driven control to suppress structural vibrations,” *Aerospace Science and Technology*, vol. 77, pp. 429–438, 2018.
- [16] Y. Zhang and X. Guan, “Active damping control of flexible appendages for spacecraft,” *Aerospace Science and Technology*, vol. 75, pp. 237–244, 2018.
- [17] M. Azimi and G. Sharifi, “A hybrid control scheme for attitude and vibration suppression of a flexible spacecraft using energy-based actuators switching mechanism,” *Aerospace Science and Technology*, vol. 82–83, pp. 140–148, 2018.
- [18] W. Niu, C. Zou, B. Li, and W. Wang, “Adaptive vibration suppression of time-varying structures with enhanced FxLMS algorithm,” *Mechanical Systems and Signal Processing*, vol. 118, pp. 93–107, 2019.
- [19] S. Mohanty and S. K. Dwivedy, “Linear and nonlinear analysis of traditional and non-traditional piezoelectric vibration absorber with time delay feedback for simultaneous resonance conditions,” *Mechanical Systems and Signal Processing*, vol. 161, article 107980, 2021.
- [20] D. Zhang and L. Zheng, “Active vibration control of plate partly treated with ACLD using hybrid control,” *International Journal of Aerospace Engineering*, vol. 2014, Article ID 432970, 12 pages, 2014.
- [21] A. Bronowicki, “A layered vibration control strategy for space telescopes, smart,” *Structures and Materials*, vol. 5056, pp. 487–496, 2003.
- [22] R. Jamshidi and A. A. Jafari, “Nonlinear vibration of conical shell with a piezoelectric sensor patch and a piezoelectric actuator patch,” *Journal of Vibration and Control*, 2021.
- [23] J. Yao, “Intelligent plate vibration control using pizeoelectric sensors and actuators,” *Proceedings of SPIE*, vol. 5253, pp. 624–629, 2003.
- [24] Z.-C. Qiu, C. Li, and X.-M. Zhang, “Experimental study on active vibration control for a kind of two-link flexible manipulator,” *Mechanical Systems and Signal Processing*, vol. 118, pp. 623–644, 2019.
- [25] F. Casella, A. Locatelli, and N. Schiavoni, “Modelling and control for vibration suppression in a large flexible structure with jet thrusters and piezoactuators,” in *Proceedings of the 39th IEEE Conference on Decision and Control (Cat. No.00CH37187)*, pp. 4491–4499, Sydney, NSW, Australia, 2000.
- [26] H. Sun, X. Tang, S. Hou, and X. Wang, “Vibration suppression for large-scale flexible structures based on cable-driven parallel robots,” *Journal of Vibration and Control*, vol. 27, no. 21–22, pp. 2536–2547, 2020.
- [27] W. Hu, Y. Gao, and B. Yang, “Semi-active vibration control of two flexible plates using an innovative joint mechanism,” *Mechanical Systems and Signal Processing*, vol. 130, pp. 565–584, 2019.
- [28] G. Shengmin and C. Hao, “A comparative design of satellite attitude control system with reaction wheel,” in *First NASA/ESA Conference on Adaptive Hardware and Systems (AHS’06)*, pp. 359–364, Istanbul, Turkey, 2006.
- [29] Z. Ismail and R. Varatharajoo, “A study of reaction wheel configurations for a 3-axis satellite attitude control,” *Advances in Space Research*, vol. 45, no. 6, pp. 750–759, 2010.
- [30] A. M. Si Mohammed, M. Benyettou, Y. Bentoutou, A. Boudjemai, Y. Hashida, and M. N. Sweeting, “Three-axis active control system for gravity gradient stabilised microsatellite,” *Acta Astronautica*, vol. 64, no. 7–8, pp. 796–809, 2009.
- [31] I. M. da Fonseca, P. M. Bainum, and A. R. da Silva, “Structural control interaction for an LSS attitude control system using thrusters and reaction wheels,” *Acta Astronautica*, vol. 60, no. 10–11, pp. 865–872, 2007.
- [32] S. Boulouma, S. Labiod, and H. Boubertakh, “Direct adaptive control of a flexible spacecraft with disturbances and uncertain actuator failures,” *Mechanical Systems and Signal Processing*, vol. 110, pp. 73–89, 2018.
- [33] B. Chen, M. Zhang, G. A. Tang, and G.-A. Tang, “Principle and experimental research on vibration reduction of flexible solar array using reaction flywheel,” *Aircraft Engineering and Aerospace Technology*, vol. 90, no. 8, pp. 1282–1287, 2018.
- [34] M. Shahravi and M. Azimi, “A hybrid scheme of synthesized sliding mode/strain rate feedback control design for flexible spacecraft attitude maneuver using time scale decomposition,” *International Journal of Structural Stability and Dynamics*, vol. 16, article 1450101, 2014.
- [35] M. Azimi, M. Shahravi, and K. Malekzadeh Fard, “Modeling and vibration suppression of flexible spacecraft using higher-order Sandwich panel theory,” *The International Journal of Acoustics and Vibration*, vol. 22, no. 2, 2017.
- [36] G. Ma, M. Xu, J. Tian, and X. Kan, “The vibration suppression of solar panel based on smart structure,” *Aeronautical Journal*, vol. 125, no. 1283, pp. 244–255, 2021.
- [37] M. Hadi, I. Mat Darus, M. O. Tokhi, and M. Jamid, “Active vibration control of a horizontal flexible plate structure using intelligent proportional-integral-derivative controller tuned by fuzzy logic and artificial bee colony algorithm,” *Journal of*

- Low Frequency Noise Vibration and Active Control*, vol. 39, pp. 1159–1171, 2019.
- [38] C. Liu, X. Yue, and Z. Yang, “Are nonfragile controllers always better than fragile controllers in attitude control performance of post-capture flexible spacecraft?,” *Aerospace Science and Technology*, vol. 118, article 107053, 2021.
- [39] C. L. Nascimento and D. W. McMichael, “Robot control using the feedback-error-learning rule with variable feedback gain,” in *1991 Second International Conference on Artificial Neural Networks*, pp. 139–143, Bournemouth, UK, 1991.
- [40] S.-J. Tsai, C.-L. Huo, Y.-K. Yang, and T.-Y. Sun, “Variable feedback gain control design based on particle swarm optimizer for automatic fighter tracking problems,” *Applied Soft Computing*, vol. 13, no. 1, pp. 58–75, 2013.
- [41] J. Wang, C. Yu, Y. Liu, D. Shen, and Y. Chen, “Variable gain feedback PD^{α} -type iterative learning control for fractional nonlinear systems with time-delay,” *IEEE Access*, vol. 7, pp. 90106–90114, 2019.
- [42] M. Heertjes, B. Hunnekens, N. V. D. Wouw, and H. Nijmeijer, “Learning in the synthesis of data-driven variable-gain controllers,” in *2013 American Control Conference*, pp. 6685–6690, Washington, DC, USA, 2013.
- [43] D. J. Leith and W. E. Leithead, “Survey of gain-scheduling analysis and design,” *International Journal of Control*, vol. 73, no. 11, pp. 1001–1025, 2000.
- [44] F. M. Caswara and H. Unbehauen, “A neurofuzzy approach to the control of a flexible-link manipulator,” *IEEE Transactions on Robotics and Automation*, vol. 18, no. 6, pp. 932–944, 2002.
- [45] V. G. Moudgal, K. M. Passino, and S. Yurkovich, “Rule-based control for a flexible-link robot,” *IEEE Transactions on Control Systems Technology*, vol. 2, no. 4, pp. 392–405, 1994.
- [46] I. Nagashima and Y. Shinozaki, “Variable gain feedback control technique of active mass damper and its application to hybrid structural control,” *Earthquake Engineering and Structural Dynamics*, vol. 26, no. 8, pp. 815–838, 1997.
- [47] Q. Guo, S. Wu, F. Liu, and G.-A. Tang, “Analysis of the affect and change rule of spacecraft flexible annex on system natural vibration characteristics (in Chinese),” *Journal of Vibration and Shock*, vol. 35, pp. 187–191, 2016.
- [48] J. Bay, “Fundamentals of linear state space systems,” *Electrical and Computer Engineering Faculty Scholarship*, vol. 3, 1999.
- [49] X. Zang, S. Wu, Q. W. Guo, and G. A. Tang, “Modal analysis and fundamental frequency optimization for a space station’s flexible solar panel (in Chinese),” *Journal of Vibration and Shock*, vol. 38, pp. 246–250, 2019.
- [50] P. Maragos, J. F. Kaiser, and T. F. Quatieri, “Energy separation in signal modulations with application to speech analysis,” *IEEE Transactions on Signal Processing*, vol. 41, no. 10, pp. 3024–3051, 1993.
- [51] A. Potamianos and P. Maragos, “A comparison of the energy operator and the Hilbert transform approach to signal and speech demodulation,” *Signal Processing*, vol. 37, no. 1, pp. 95–120, 1994.
- [52] R. Dillon, “Classifying musical performance by statistical analysis of audio cues,” *Journal of New Music Research*, vol. 32, no. 3, pp. 327–332, 2003.
- [53] S. Baloch, S. Z. Jamali, K. K. Mehmood et al., “Microgrid protection strategy based on the autocorrelation of current envelopes using the squaring and low-pass filtering method,” *Energies*, vol. 13, pp. 1–13, 2020.
- [54] T. W. Parks and C. S. Burrus, *Digital Filter Design*, Wiley-Interscience, 1987.